BIOMATERIALS

Wirelessly steerable bioelectronic neuromuscular robots adapting neurocardiac junctions

Hiroyuki Tetsuka[1,2], Samuele Gobbi[3], Takaaki Hatanaka[1,2], Lorenzo Pirrami[3], Su Ryon Shin[1]*

Biological motions of native muscle tissues rely on the nervous system to interface movement with the surrounding environment. The neural innervation of muscles, crucial for regulating movement, is the fundamental infrastructure for swiftly responding to changes in body tissue requirements. This study introduces a bioelectronic neuromuscular robot integrated with the motor nervous system through electrical synapses to evoke cardiac muscle activities and steer robotic motion. Serving as an artificial brain and wirelessly regulating selective neural activation to initiate robot fin motion, a wireless frequency multiplexing bioelectronic device is used to control the robot. Frequency multiplexing bioelectronics enables the control of the robot locomotion speed and direction by modulating the flapping of the robot fins through the wireless motor innervation of cardiac muscles. The robots demonstrated an average locomotion speed of ~0.52 ± 0.22 millimeters per second, fin-flapping frequency up to 2.0 hertz, and turning locomotion path curvature of ~0.11 ± 0.04 radians per millimeter. These systems will contribute to the expansion of biohybrid machines into the brain-to-motor frontier for developing autonomous biohybrid systems capable of advanced adaptive motor control and learning.

INTRODUCTION

Living organisms have programmed complex motor patterns and efficient actuating systems through evolution to interface their movement with external/internal environmental cues, which are in dynamic and nonequilibrium states. The natural paradigms of biological systems have inspired several researchers to focus on developing tissue-engineered biohybrid machines that can swim (*1*–*5*), walk (*6*–*8*), pump (*9*, *10*), and grip (*11*) by integrating contractile living cardiac or skeletal muscles and artificially pliable components. These biohybrid systems can replicate life-like biomimetic behaviors and functions, such as jellyfish-like stroke kinetics (*2*), the motion mechanism of antagonistic muscles (*11*), heart-like pumps (*10*), cardiac mechanoelectrical signaling (*1*), and organ-on-a-chip platforms (*12*), whose design principles and functions will foster various applications in the biomedical and soft robotics fields. Despite effectively replicating various biological behaviors and functions, most current biohybrid machines present difficulties in incorporating real-time perception, response, and adaptability to their internal/external environment because of the lack of a nervous system. Another biohybrid approach to incorporating adaptive perception is the artificial enhancement of live animals, such as cockroaches, beetles, and jellyfish (*13*–*16*). Although these augmented animals can have the inherent adaptive behaviors of animals, the bottom-up tissue engineering method could avoid using animals and assemble cellular building blocks with desired functions to construct biohybrid robots with autonomous functionality.

Biological motions rely on the nervous system to interface movement with the surrounding environmental cues. The central nervous system controls skeletal muscle contractions via motor neurons (MNs) to link thoughts with body movements (*17*). As a component of the peripheral nervous system, the autonomic nervous system controls the contraction of cardiac and smooth muscles in the heart and visceral organs. This system regulates blood flow throughout the cardiovascular system and helps to control the digestive and respiratory systems, urinary tract, and secretion (*18*, *19*). In the heart, the heartbeat is derived from rhythmic pacing discharges from the sinoatrial node. However, the autonomic nervous system regulates the heart rate and contractility through sympathetic and parasympathetic neurons, as well as the endocrine system. These neural pathways respond rapidly to changes in body tissue requirements and are only relevant for the vertebrate system. As such, incorporating such a nervous system into the biohybrid platform enhances advanced motor behaviors in biohybrid machines, akin to those observed in organisms. This integration facilitates autonomous navigation, allowing these machines to detect their surroundings and dynamically adjust movement patterns. This capability holds substantial promise across diverse applications in the robotic and biomedical fields.

Recently, Aydin *et al.* (*20*, *21*) demonstrated a biohybrid swimmer operated by the neuromuscular junctions of skeletal muscles and MNs. The light stimulation of cocultured optogenetically modified MNs induced this machine's motility via chemical synapses established between the muscle fibers and the motor nerves. Nonetheless, limitations persist in terms of controllability of robot motions and robustness of cell signaling because of the lack of an onboard control system and patterned neuron firing, as well as the depletion of neurotransmitter vesicles at the neuromuscular junctions. Incorporating electrical synapses, which are mediated by ionic flow via gap junctions instead of neurotransmitters, into neuromuscular robots with wireless bioelectronic technologies may offer advantages for the development of next-generation neuromuscular biohybrid robots with extended muscle responsiveness and controllability. Neural networks could be wirelessly and selectively activated through direct and local electrical signals using electrodes patterned into bioelectronic devices to control the activity of electrically isolated muscle tissue patches assembled on a biohybrid machine through electrical synapses. Such selective muscle tissue

[1]Division of Engineering in Medicine, Department of Medicine, Brigham and Women's Hospital, Harvard Medical School, 65 Lansdowne Street, Cambridge, MA 02139, USA. [2]Research Strategy Office, Toyota Research Institute of North America, Toyota Motor North America, 1555 Woodridge Avenue, Ann Arbor, MI 48105, USA. [3]iPrint Institute, HEIA-FR, HES-SO University of Applied Sciences and Arts Western Switzerland, Fribourg 1700, Switzerland.
*Corresponding author. Email: sshin4@bwh.harvard.edu

activation via the localized wireless electrical stimulation of neurons and subsequent fast and robust signal transmission will facilitate the design and integration of controllable muscle actuator arrays into engineered neuromuscular systems.

Within the native system, the autonomic nervous system communicates with cardiac muscles through a chemical synapse characterized by unidirectional signaling and mediated by neurotransmitters. The most familiar neurotransmitters released by neurons of the autonomic nervous system are acetylcholine and norepinephrine (*22*). Although all preganglionic neurons of the autonomic nervous system release acetylcholine, most postganglionic sympathetic neurons secrete norepinephrine, and all postganglionic parasympathetic neurons secrete acetylcholine. These neurotransmitters are synthesized in the axon terminals and stored in vesicles for subsequent release. In the neurocardiac junctions of cardiac muscles and sympathetic/parasympathetic postganglionic neurons (Fig. 1A), norepinephrine released by the postganglionic sympathetic neurons binds to the adrenergic receptors in the myocardium and is excitatory. However, acetylcholine released by the postganglionic parasympathetic neurons binds to the muscarinic receptors and is inhibitory. These antagonistic postganglionic sympathetic and parasympathetic neurons regulate the heart rate: Sympathetic stimulation increases the heart rate and myocardial contractility under emotional arousal and various pathological conditions, whereas parasympathetic stimulation decreases the heart rate under restful conditions. The neurotransmitter activity is terminated through the enzymatic degradation of acetylcholine or norepinephrine reuptake into the sympathetic axon terminal.

In this Research Article, we demonstrate the integration of electrical synapses of human induced pluripotent stem cell–derived (iPSC) MNs and iPSC-cardiomyocytes (CMs) into a biohybrid machine instead of a chemical synapse (Fig. 1B) and present the neuronal control of wirelessly powered biohybrid robots with frequency multiplexing bioelectronics. The electrical synapse enables a connection between different cell types via a gap junction and faster bidirectional signaling, which can expand the flexibility of designing biohybrid systems and producing versatile biohybrid machines. Expanding the scope of designing and modeling neuromuscular systems will increase the accessibility of biohybrid robotics, enabling their use as robotic systems and fundamental research. In our robotic design, the frequency multiplexing wireless system serves as an artificial brain and controls selective neural activation to initiate neuromuscular robot fin motions through signal transduction from iPSC-MNs to iPSC-CMs via the electrical synapse (movie S1). Cardiac muscle activity is innervated and evoked through electrically stimulated iPSC-MNs, which will expand CM-based biohybrid machines into a sensory-motor frontier. Wireless bioelectronics is proposed as a promising platform for electronic skins (*23*–*25*) and neuromodulators (*26*, *27*) and offers an innovative strategy for locally stimulating cells on biohybrid robots (*5*). We demonstrate selective neural activation by implementing a frequency multiplexing technique, shown in multiple-actuator control (*28*–*30*), into bioelectronic neuromuscular robots. This method is based on wireless power transmission and resonance-driven selectivity for the targeted stimulation of neurons, enabling multiple signals at nonoverlapping frequency bands to be simultaneously sent. This study sends two modulation signals comprising frequency, pulse duration, and pulse interval information at 6.78 and 13.56 MHz over the frequency multiplexing system. The two modulation signals are induced to two resonant coils on a bioelectronic device through magnetic coupling between the wireless bioelectronic device and the excitation circuits, generating voltage pulses that electrically stimulate the iPSC-MN tissues constructed on each resonant coil. The frequency multiplexing bioelectronics controls the robot's locomotion speed and steering by independently modulating its left and right fins.

RESULTS

Motor neurocardiac junction formation

An electrical synapse via gap junctions exists temporarily between myocytes and neurons before a chemical synapse is established in vivo (*31*, *32*). These electrical synapses allow electrical coupling between adjacent cells by passing ions through junctional pores and constitute a transient mechanism of cellular communication. We used a microfluidic device to form electrical synapses by coculturing iPSC-MNs and iPSC-CMs and examined their motor innervation

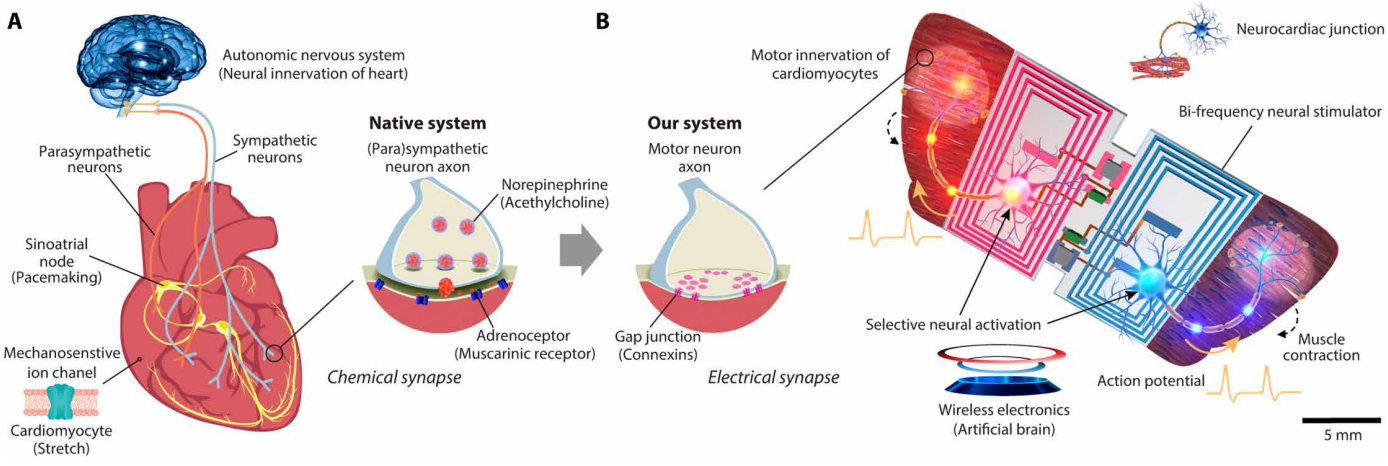

Fig. 1. Wirelessly controllable bioelectronic neuromuscular robots for steering actuation behavior. (**A**) Dynamic control of the heart via the neural innervation of CMs. (**B**) Schematic of a bioelectronic neuromuscular robot with selective motor innervation of CMs driven by a wireless frequency multiplexing bioelectronic device. Scale bar, 5 mm.

functionality in cardiac muscles in vitro (Fig. 2A). We selected iPSC-CMs and iPSC-MNs as model cell sources for our biohybrid system. Human iPSC-CMs can generate consistent contractile forces over a long period compared with neonatal rat CMs and other cell sources (*1*, *5*, *33*). Furthermore, human-derived stem cells are abundant sources for applications in tissue engineering, high-throughput drug screening, and regenerative medicine (*34*) and can be better cell sources for the scale-up construction of biohybrid machines while avoiding the ethical issues associated with animal euthanasia. Compartmentalization is ensured by seeding iPSC-CMs in one chamber of the device, followed by a 5-day incubation to form a mature syncytial layer. On day 6, iPSC-MNs were seeded in the opposite chamber of the fluidically separated device. The volumetric gradient induced the migration of iPSC-MN axons through microchannels into the iPSC-CM compartment (Fig. 2B), where they were physically associated with iPSC-CMs and clusters of connexin 43 (Cx43) on iPSC-CMs (Fig. 2C and figs. S1A and S2). The observation of varicosities also strengthened the evidence of physical contact with iPSC-CMs (fig. S2A), because varicosities indicate the transformation of the growth cone into a synaptic terminal after postsynaptic cell contact (*35*, *36*). Because the Cx-generated gap junctions mediate electrical coupling though ion transfer (Fig. 2D), Cx represents an essential clue for gap junction–mediated neurocardiac junctions. Three principal Cxs—Cx43, Cx40, and Cx45—are expressed in CMs, where Cx43 is dominant at gap junctions and is typically associated with direct cell-to-cell communication through the interconnection among Cx43 clusters. Cx26, Cx36, and Cx43 are expressed across the MNs (*37*–*39*). Neurons typically form gap junctions with astrocytic Cx43 via Cx (*40*). Cx43 was expressed in iPSC-MNs and iPSC-CMs (Fig. 2E and fig. S1B) and could form plaques of intercellular channels.

We characterized the functionality of motor neurocardiac junctions via membrane potential imaging. The iPSC-MN–iPSC-CM signal transduction was visualized under the electrical stimulation of iPSC-MNs or iPSC-CMs on day 20 of coculturing. Figure S3 shows the electrical stimulation conditions for iPSC-MNs and iPSC-CMs. We stimulated the iPSC-MNs by applying a pulsed voltage of ~1 V/mm (pulse duration, 0.2 ms; and frequency, 100 Hz). Applying a pulsed voltage, as theoretically calculated using a leaky integrate-and-fire model, initiated stable continual neuronal firing (fig. S4). The iPSC-MNs showed a typical branched morphology and sufficient network connectivity after culturing for ~10 days (fig. S5, A and B). The electric field threshold of iPSC-MNs was ~0.6 V/mm when stimulated by an anodal monophasic pulsed voltage (pulse duration, 0.2 ms) using a pair of electrodes (fig. S5C). The electrical activities of iPSC-MNs followed well the applied electric field signal

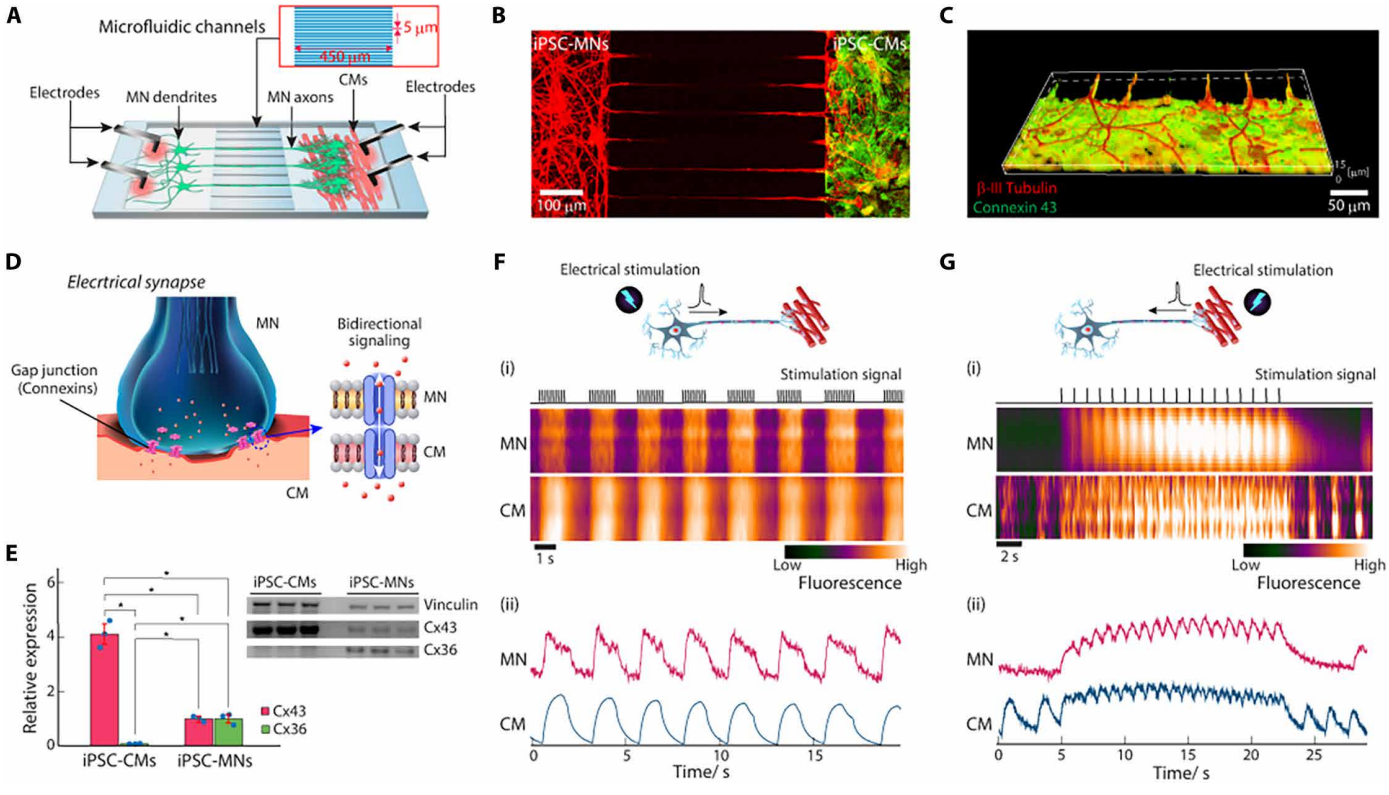

Fig. 2. Signal transduction between iPSC-MNs and iPSC-CMs. (**A**) Schematic depiction of the microfluidic device used to test the functionality of neurocardiac junctions. (**B**) Confocal image of immunostained iPSC-MNs (red, β-III tubulin) and iPSC-CMs (green, sarcomeric α-actinin) in the microfluidic device on day 20. Scale bar, 100 μm. (**C**) 3D reconstructed images of confocal images of immunostained iPSC-MN axons/iPSC-CM junctions in the iPSC-CM compartment (red, β-III tubulin; green, Cx43). Scale bar, 50 μm. (**D**) Schematic illustration of the electrical synapse between the MN and CM. Gap junctions allow the current to pass directly between neighboring cells by passing ions through the Cx pores to neighboring cells. (**E**) Relative expression levels of Cx43/Cx36 in iPSC-MNs and iPSC-CMs, evaluated by Western blotting after 10 days (iPSC-CMs) and 15 days (iPSC-MNs) of culture ($n = 3$ samples; data represent mean ± SEM, $^*P < 0.01$). The Cx43/Cx36 expression levels in iPSC-CMs are shown relative to those in iPSC-MNs. (**F** and **G**) Kymograph images (i) and traces (ii) of the temporal membrane potential changes in the iPSC-MNs and iPSC-CMs at the ROI for each chamber of the microfluidic device in response to the electrical stimulation of iPSC-MNs (F) or iPSC-CMs (G). Scale bars, 1 s (F) and 2 s (G).

under these conditions, as shown in the membrane potential dynamics over time in response to the applied electric field (fig. S5, D and E, and movie S2).

To analyze the signal transduction from electrically stimulated iPSC-MNs to iPSC-CMs, we traced the temporal membrane potential changes, which indicate neural and cardiac depolarization, in the iPSC-MNs and iPSC-CMs at the corresponding region of interest (ROI) of fig. S6 in response to the electrical stimulation of iPSC-MNs (Fig. 2F and movie S3). The electrical activities of the iPSC-CMs were well synchronized with those of the electrically stimulated iPSC-MNs, as shown in the kymograph images (Fig. 2, F-i) and plots (Fig. 2, F-ii), confirming the motor innervation of cardiac muscles. We observed that the iPSC-MN–iPSC-CM signal transduction was bidirectional, a characteristic of electrical synapses (Fig. 2G). The iPSC-MNs showed synchronized electrical activities with those of electrically stimulated iPSC-CMs. Furthermore, administering the gap junction blocker carbenoxolone inhibited the iPSC-MN–iPSC-CM signal transduction (fig. S7), indicating that the iPSC-MN–iPSC-CM signaling pathway is an electrical synapse mediated by gap junctions. Electrical activities between the iPSC-MNs and the iPSC-CMs were not synchronized in the spontaneous-firing state because of the random firing and the low firing rate of neurons (fig. S8) (*41*). However, repetitive electrical stimulation can elicit the repetitive firing of neurons with an increased firing frequency, instructing the stimulation-evoked response of the cardiac muscles. No phase lag between stimulation input, neuron firing, and cardiac muscle contraction was recorded because the propagation velocity (~100 m/s) of the action potentials in neurons is much higher than that of a typical fluorescence measurement setup (video frame rate, 40 fps; and barrier between the iPSC-MNs and iPSC-CMs compartments in a microfluidic device, 450 μm). We also numerically calculated the electric field potential in the microfluidic device to determine the potential of electrically stimulating iPSC-CMs through electrodes placed in the iPSC-MN culturing chamber. The electric field potential was not distributed over the microchannels (fig. S9A). We experimentally confirmed that a 0.2-ms pulse width electrical signal at 10 to 100 Hz used for iPSC-MN stimulation did not depolarize the iPSC-CMs because of their chronaxie variance (fig. S9B). Neurons typically exhibit chronaxies between 0.1 and 0.4 ms (*42*, *43*), whereas the CM shows a higher chronaxie of ~2 ms (*44*, *45*). We observed a much higher threshold pulse duration of ~50 ms for iPSC-CMs to be depolarized compared with that for iPSC-MNs (~0.2 ms).

Neuromuscular robots integrated with a wireless frequency multiplexing bioelectronic device

We implemented motor neurocardiac junctions into a flexible wireless circuit to build a wireless bioelectronic neuromuscular robot. The envisaged neuromuscular robot comprises a wireless device whose edges are integrated with soft carbon nanotube (CNT)/gelatin thin film scaffolds and a tissue-engineered bilayer (iPSC-MNs–iPSC-CMs) constructed onto the wireless bioelectronic device (total of four layers, Fig. 3A). We designed the neuromuscular robots by optimizing the fin shape and the cardiac muscle alignment on the fins based on finite-element simulations (fig. S10 and Supplementary Methods). To generate a large deflection and induce a delay in the deformation relaxation of hydrogel fins, a

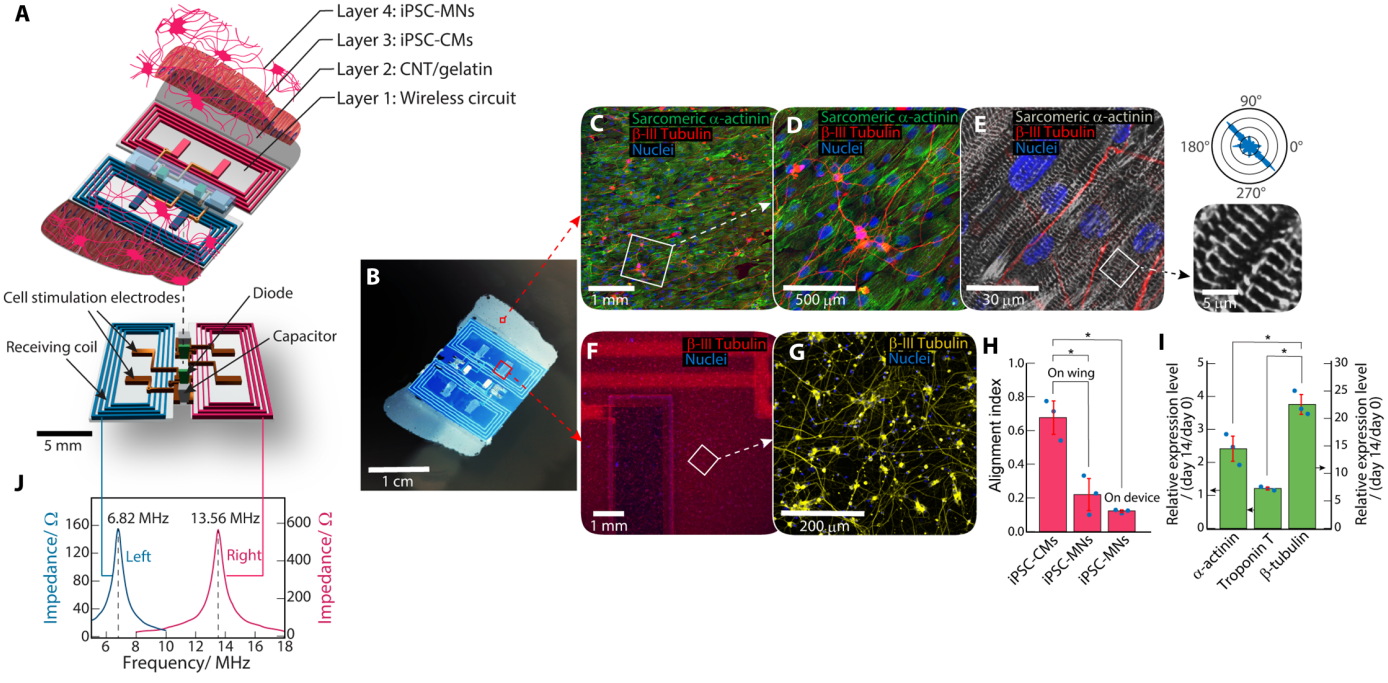

Fig. 3. Fabrication of bioelectronic neuromuscular robots. (**A**) Layer-by-layer structure of a biohybrid neuromuscular robot comprising four layers. Scale bar, 5 mm. (**B**) Photograph of the fabricated biohybrid neuromuscular actuator. Scale bar, 1 cm. (**C** to **E**) Confocal images of the immunostained cocultured iPSC-MNs and iPSC-CMs on the fin. Scale bars, 1 mm (C), 500 μm (D), 30 μm (E), and 5 μm [expansion of (E)]. (**F** and **G**) Confocal images of the immunostained iPSC-MNs on the bioelectronic device. Scale bars, 1 mm (F) and 200 μm (G). (**H**) Comparison of alignment index for cultured iPSC-MNs and iPSC-CMs on the fin and the bioelectronic device ($n = 3$ samples; data represent mean ± SEM, $^*P < 0.01$). (**I**) Relative protein expression levels of α-actinin, troponin T, and β-tubulin of the iPSC-MNs and iPSC-CMs on the robot on day 14 to the iPSC-MNs and iPSC-CMs on day 0 ($n = 3$ samples; data represent mean ± SEM, $^*P < 0.01$). (**J**) Resonant frequencies for the left and right coils.

butterfly wing–shaped fin structure with a muscle alignment of 90° to the device boundary was adopted. This structural design was estimated to have a large, localized deformation ability of fins. The component layers of the wireless bioelectronic device included a flexible printed circuit board (PCB) comprising receiver coils, neural cell stimulation electrodes, bonding pads for diodes and capacitors separated by a polyimide (PI) film, electronic components of diodes and capacitors, and an encapsulation layer of polydimethylsiloxane (PDMS) to isolate the electronic components from the aqueous medium (fig. S11). We generated the neutral buoyancy by optimizing the thicknesses of the PDMS encapsulation layer of the electronic components (1000 μm thick) and the PDMS device coating layer (50 μm thick) (fig. S12). Their density was calculated to be ~1069 ± 51 kg/m^3, comparable to that of the working medium (~1050 kg/m^3). The wireless device–embedded CNT/gelatin scaffold body floated when immersed in a medium (fig. S12B). A 100-μm-thick CNT/gelatin thin film with a nanosurface pattern was engineered by the enzymatic cross-linking of the CNT-dispersed gelatin prepolymer solution using a microbial transglutaminase (figs. S13 and S14A), followed by transferring patterns using a PDMS stamp with a 0.8-μm groove width and depth (fig. S14, B and C) to self-assemble the iPSC-CMs as engineered muscular tissues with uniaxial cellular alignment. The CNT/gelatin thin films with the nanosurface pattern were integrated with the wireless bioelectronic device using hinges. We adopted a 0.1 w/v% CNT/10 w/v% gelatin hydrogel with Young's modulus of ~170 kPa to minimize hydrogel degradation for long-term cultivation (*46*, *47*) and enhance robot actuation performance by increasing the mechanical stiffness of hydrogel by incorporating CNT (fig. S14, D and E). This mechanical stiffness can induce a strong deflection of the hydrogel (movie S4), where the CNT/gelatin hydrogel film with a cocultured iPSC-MN–iPSC-CM construct exhibited a stronger actuation performance than the pristine gelatin film–based actuator.

To establish a coculture of iPSC-MNs and iPSC-CMs in vitro, we optimized the surface coatings and culture medium to allow both cell types to mature in concert (figs. S15A and fig. S16A). We observed that adding the iPSC-MN culture medium rapidly increased the beating rate (fig. S16B) and, subsequently, detached iPSC-CM over time, whereas the iPSC-MNs remained viable in all coculturing medium compositions (fig. S15B). After culturing the iPSC-CMs in the iPSC-CM monoculture medium until an electrically connected syncytial layer was formed, we opted to plate the iPSC-MNs in a standard iPSC-MN medium on day 5 for 4 days, at which point the iPSC-MNs already displayed robust neurite branching. On day 9, the medium was replaced with a standard iPSC-CM medium. Under this protocol, the iPSC-MNs and iPSC-CMs seeded as a single suspension showed typical neural and muscle activities (fig. S16, B and C) and maintained viability and adherence (fig. S16D). The MN/CM hybrids exhibited a three-dimensional (3D) structure comprising tangled interconnected MN networks and CMs (fig. S17) and strong synchronous and spontaneous beating (movie S5). This protocol seeded the iPSC-CMs onto robot CNT/gelatin scaffolds. On day 5, the iPSC-MNs were cocultured onto the entire construct to confirm neurocardiac junction formation between the iPSC-MNs and iPSC-CMs on the CNT/gelatin scaffold. An ~30-μm-thick tissue construct comprising random iPSC-MN networks and aligned iPSC-CM cardiac tissue was formed on the CNT/gelatin fin (Fig. 3, B to H, and fig. S18). The resulting cocultures showed expression of the MN marker β-tubulin and the CM marker α-actinin. The β-tubulin and α-actinin expression levels on the construct increased with time (Fig. 3I). The resultant ~150-μm-thick CNT/gelatin fins of the robots started detaching spontaneously from the glass substrate after ~day 10 and showed strong actuation behavior (movie S6).

Wireless frequency multiplexing system

The frequency selectivity and separation of the resonant coils in a wireless bioelectronic device are sufficiently high to allow the proper operation of bioelectronic devices to demonstrate the independent activation between the iPSC-MN tissues constructed on the left and right fins (Fig. 3J). The bioelectronic device can generate sufficient electric fields up to ~2 mm above the neural cell stimulation electrodes to selectively stimulate the iPSC-MN tissues on the device's left and right coils (fig. S19). The developed wireless bioelectronic device is operated with planar inductors and surface mount device capacitors, forming two inductor-capacitor (LC) circuits tuned at two resonant frequencies to control robot motion via cardiac muscle innervation (fig. S20). LC circuits produce a dc voltage through a voltage rectifier circuit when exposed to an ac magnetic field with a frequency that matches the resonant frequency of the circuits (F_{RC}). This DC voltage is applied to neural cells via electrodes to stimulate the iPSC-MNs represented by a resistor (R_{CELLs}) in the electrical model. The two LC circuits are designed to have different F_{RC} values at 6.78 MHz (left coil) and 13.56 MHz (right coil) (fig. S21). After that, each circuit can be independently or simultaneously activated by using two power amplifiers (PAs) that can modulate the envelope of the radio frequency (RF) signals using an on-off keying modulation scheme. Adjusting the pulse width and excitation interval time produces on-off patterns relevant for the electrical stimulation of neurons to control robot motion.

Electrical signals were transmitted through a parallel double-frequency transmitter based on current-mode class-D PAs (Fig. 4A and fig. S22) into a bifrequency wireless bioelectronic device. The two PAs inject sinusoidal alternating currents at 6.78 and 13.56 MHz into the excitation coils. Each excitation coil transmits an AC signal at a frequency that matches the f_{RC} to the bioelectronic device. The voltage rectifiers in the bioelectronic device convert each ac voltage into a dc voltage to activate neurons. The voltage output from the bioelectronic device between the parallel double-frequency transmitters depends on the distance between each transmitter coil and the device (fig. S23). When the distance between the coils is 30 mm, a plane 5 mm above the lower coil has a uniform voltage output distribution at frequencies of 6.78 and 13.56 MHz (Fig. 4B). Figure 4C highlights the generation of monophasic pulse voltages with a pulse width of 0.2 ms generated using the wireless bioelectronic device for stimulating neural cells. Voltages of ~6 V, which are well above the threshold voltage for inducing neural activation, can be generated. The output voltage from the bioelectronic device can be controlled in the range of ~2 to 6 V by adjusting the PA voltage (V_{sup}), which is proportional to the output voltage (Fig. 4D). Wireless power transfer relies on high-frequency magnetic coupling in industrial, scientific, and medical bands (6.78 and 13.56 MHz) to avoid signal losses from biofluid absorption. Voltage signal transmission was not attenuated through the medium (fig. S24).

Wireless control of bioelectronic neuromuscular robots

When the neuromuscular robot was immersed in the medium in a 100-mm-diameter petri dish placed between the excitation coils (fig. S25) and 2.5 V was applied to the PA, the robot fins flapped up

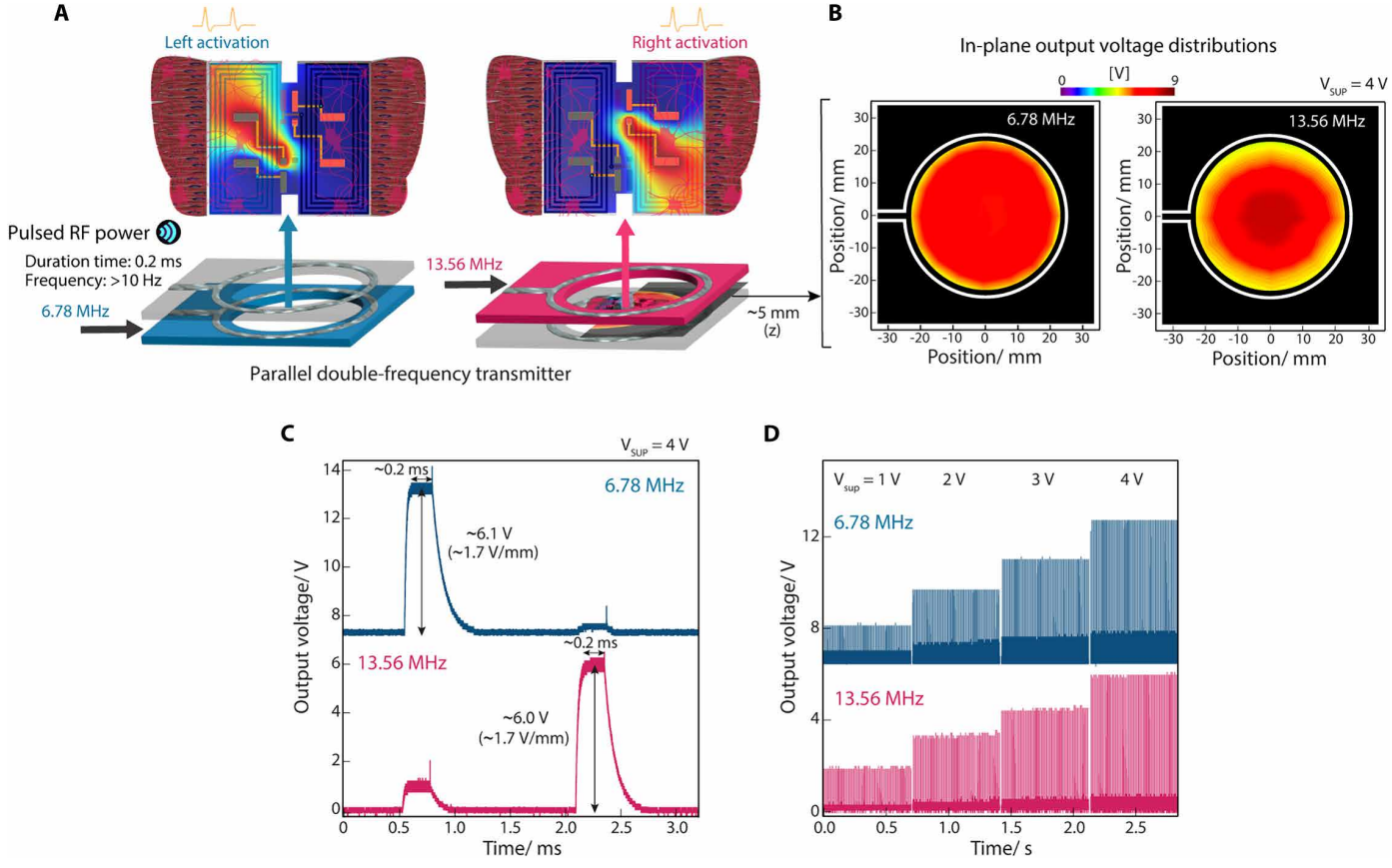

Fig. 4. Wireless frequency multiplexing system and RF power transfer. (**A**) Schematic of the electrical stimulations of a neuromuscular robot through a parallel double-frequency transmitter. (**B**) In-plane output voltage distributions when the flexible PCB-based wireless bifrequency bioelectronic device was placed ~5 mm above the two PAs (V_{sup} = 4 V). (**C**) Output voltage signals from the wireless bioelectronic device under signal transmission with a duration time of 0.2 ms and a frequency of 100 Hz at 6.78 and 13.56 MHz (V_{sup} = 4 V). (**D**) Power amplifier voltage dependencies on output voltages. The output voltage increases linearly with the PA voltage.

and down because of the wirelessly transmitted neural activation signals (Fig. 5, A and B, and movie S7). The induced electrical signals stimulate the neurons (iPSC-MNs) first, followed by signal transduction to the cardiac muscles (iPSC-CMs) via a gap junction, resulting in cardiac muscle contraction and fin flapping. A threshold amplifier voltage to drive the robots was 2.5 V, and we used the voltage to evaluate actuation and locomotion performance of robots to avoid cell overstimulation and electrode degradation because of the generation of gases caused by water electrolysis. Figure 5C compares the threshold voltages to initiate cardiac muscle contraction in the neurocardiac and cardiac muscle–only systems. Although no substantial differences were observed in deflection performance or swimming speed (fig. S26), we observed a considerably decreased threshold voltage to initiate cardiac muscle contraction through the upstream stimulation of neurons for the neurocardiac system, compared with that by the direct stimulation of cardiac muscles for the cardiac muscle–only system. The decreased threshold voltage for the neurocardiac system manifests the efficient motor innervation of cardiac muscles. The neurocardiac system could also reduce power consumption compared with the cardiac muscle–only biohybrid system. We controlled the cardiac muscle contraction with regularities via neurons by preparing arbitrary waveforms as modulation signals using a custom-made MATLAB script (fig. S27), where two rectangular pulses (pulse width, 0.2 ms; and repeat frequency, 10 Hz) at 6.78 and 13.56 MHz bands were repeated in arbitrary on-off intervals. These signals enable the cardiac muscles to actuate at arbitrary rates (0.5 to 3.0 Hz) via signal transmission from the neurons. Optical flow and video analyses revealed that the fin was lifted upward upon initiating cardiac muscle contraction, with their deflection reaching a maximum angular displacement of ~40° at ~0.3 s (Fig. 5B). It then gradually relaxed and returned to its original state in ~0.6 s. The maximum passive level of bending in the fins induced by the cardiac muscle passive tension force was ~2.2 ± 0.19 mm (fig. S28). Hydrogel's actuation dynamics enabled the wireless control of the robot fin-flapping speed up to 2.0 Hz. The limitation on the flapping rate is due to the delayed relaxation-contraction behavior of muscle tissue induced by hysteresis in the actuation response of the hydrogel scaffold, in particular for large-sized tissue constructs. As shown in Fig. 5B, the robot fins take ~0.6 s to completely relax and cannot keep up with the cardiac cell contraction rate above 2 Hz because the next contraction occurs before the fins relax. The robots maintained their signal transduction performance and retained ~82% of their initial angular displacement even after 5-week periods (Fig. 5D). This result implies that cell integrity and its contractile and signaling performance can be preserved over time by integrating wireless bioelectronic devices and local electrical

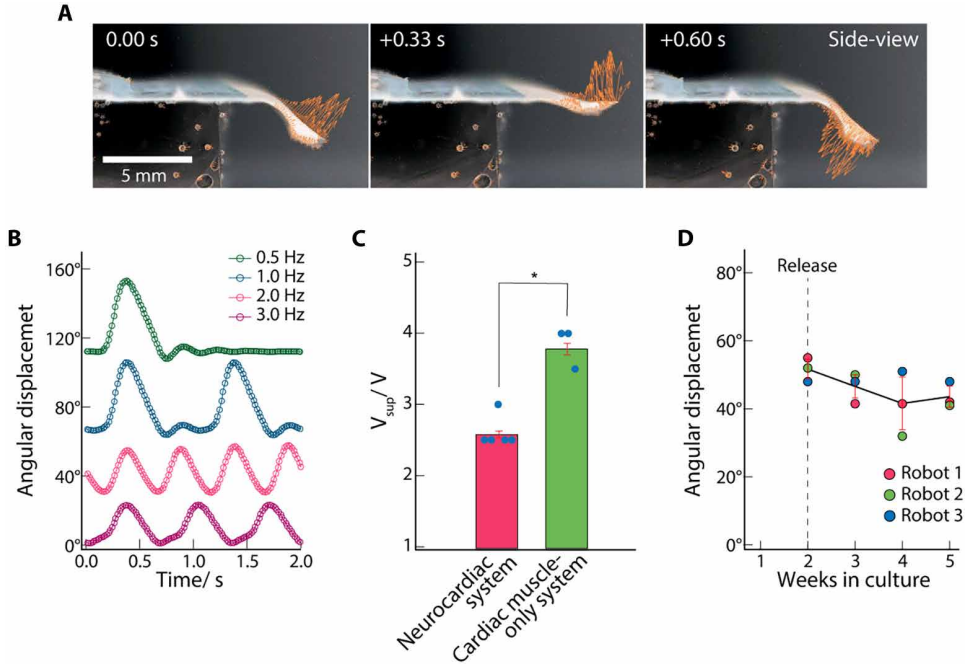

Fig. 5. Actuation behaviors of bioelectronic neuromuscular robots. (**A**) Optical flow analyses of the neuromuscular robot fin highlighting the production of alternating upward and downward vectors during an ~1-Hz pacing (V_{sup} = 2.5 V). Each orange arrow indicates motion direction and magnitude. Scale bar, 5 mm. (**B**) Angular displacements of the robot fin at different pacing frequencies (V_{sup} = 2.5 V). (**C**) A comparison of the threshold voltages to initiate cardiac muscle contraction in the neurocardiac and cardiac muscle–only systems (n = 5 robots for the neurocardiac system, n = 3 robots for the cardiac muscle–only system; the data represent the mean ± SEM, *P < 0.01). (**D**) Actuation performance of robots for 5 weeks (n = 3 robots; data represent mean ± SEM). Solid black line shows the average angular displacement of the robot fin traced during ~1-Hz pacing (V_{sup} = 2.5 V) for three robots. All actuation behaviors were analyzed for the robots placed and attached to a PDMS block in the medium to avoid the influence of the robot's forward locomotion.

stimulation. The long-term durability is much higher than that of other neonatal rat CMs or skeletal muscle–based biohybrid robots (table S1). Two signals are multiplexed to be interdigital or time-differentially generated to control the left and right fins through the individual control of neural stimulation (Fig. 6A). Interdigital signal multiplexing triggered a synchronized flapping of fins (movie S8). However, time-differential multiplexing enabled the alternate flapping of fins (movie S9). The signals from the left and right coils at two frequencies can be separately or simultaneously switched (fig. S29). Figure 6B and movie S10 demonstrate the individual actuation control of the left and right fins by switching the transmitting signal mode and interval. Moreover, by switching the transmitting signal mode, interval, and frequency, the left and right fin-flapping speed and timing were individually controllable and manipulatable (fig. S30 and movie S11), indicating the high selectivity of the developed localized electrical stimulation–incorporated bioelectronic strategy. Electrical synapses also provide robust cell signaling. The robustness of signaling between the iPSC-MNs and the iPSC-CMs via electrical synapses is shown in fig. S31. A controlled steady robot fin deflection due to muscle contraction was sustained over 150 s, much longer than that of the neuromuscular robot propelled via chemical synapses (~20 s, after which muscles began to fatigue, and the robot decelerated because of the depletion of neurotransmitters) (*20*), demonstrating the robustness of our system.

Locomotion performance of bioelectronic neuromuscular robots

The structural design of fins and soft hydrogel properties generate undulatory deformation dynamics, facilitating the robot's forward propulsion (fig. S32A). After muscle contraction and relaxation, the fins deform in a large wavelike fashion, resulting in a slight delay in robot fin deflection (fig. S32B and movie S12). Figure 7A shows the forward locomotion performance of the robot. The robot was kept within 25 mm of the center of the petri dish to track its locomotion through a view hole of excitation coils. We assume that the robot experiences a negligible wall effect for this condition, as revealed by computational fluid dynamic analysis (fig. S33). The robot locomotion speed and angle were changed by swapping the signal transmitting modes and frequencies (movie S13). Although efficient forward locomotion of the robots was achieved by alternately flapping their left and right fins at time-differential mode I in Fig. 7A (locomotion speed, ~0.57 mm/s), the simultaneous fin flapping impeded efficient forward propulsion (locomotion speed, ~0.11 mm/s at II and ~0.12 mm/s at III). It changed the locomotion angle (angle change, ~29° at II and ~23° at III) according to the transmitted signal frequencies at interdigital modes II and III in Fig. 7A. In alternating fin flapping, the direction of fluid displaced by the upward flapping of one fin coincides with the direction of fluid displaced by the downward relaxation of the other fin (Fig. 7B, fig. S34A, and movie S14), producing efficient forward propulsion. However, the simultaneous flapping of the fins generates countercurrent fluid flow toward the robot body, suppressing forward propulsion and consequently reducing linear displacement (fig. S34B). Alternate fin flapping yielded an average robot locomotion speed of ~0.52 ± 0.22 mm/s (Fig. 7C). By adjusting the flapping mode to time-differential and frequencies on both fins (left fin, 1 Hz; and right fin, 2 Hz for a left turn; and left fin, 2 Hz; right fin, 1 Hz for a right turn), the robots exhibited

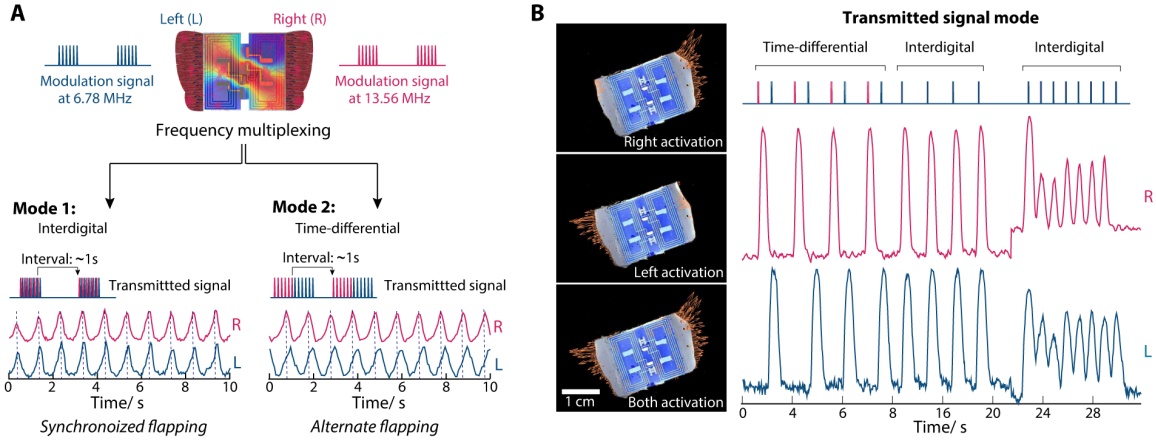

Fig. 6. Wireless control of bioelectronic neuromuscular robots. (**A**) Input signal mode dependencies on the actuation timing of the fins. (**B**) Optical flow analyses when the right and left fins were separately activated at different times. Each orange arrow in the optical flow images indicates motion direction and magnitude. The plots show fin deflections at each input signal (V_{sup} = 2.5 V). The controllability of the robots was analyzed for the robots placed and attached to a PDMS block in the medium to avoid the influence of the robot's forward locomotion. Scale bar, 1 cm.

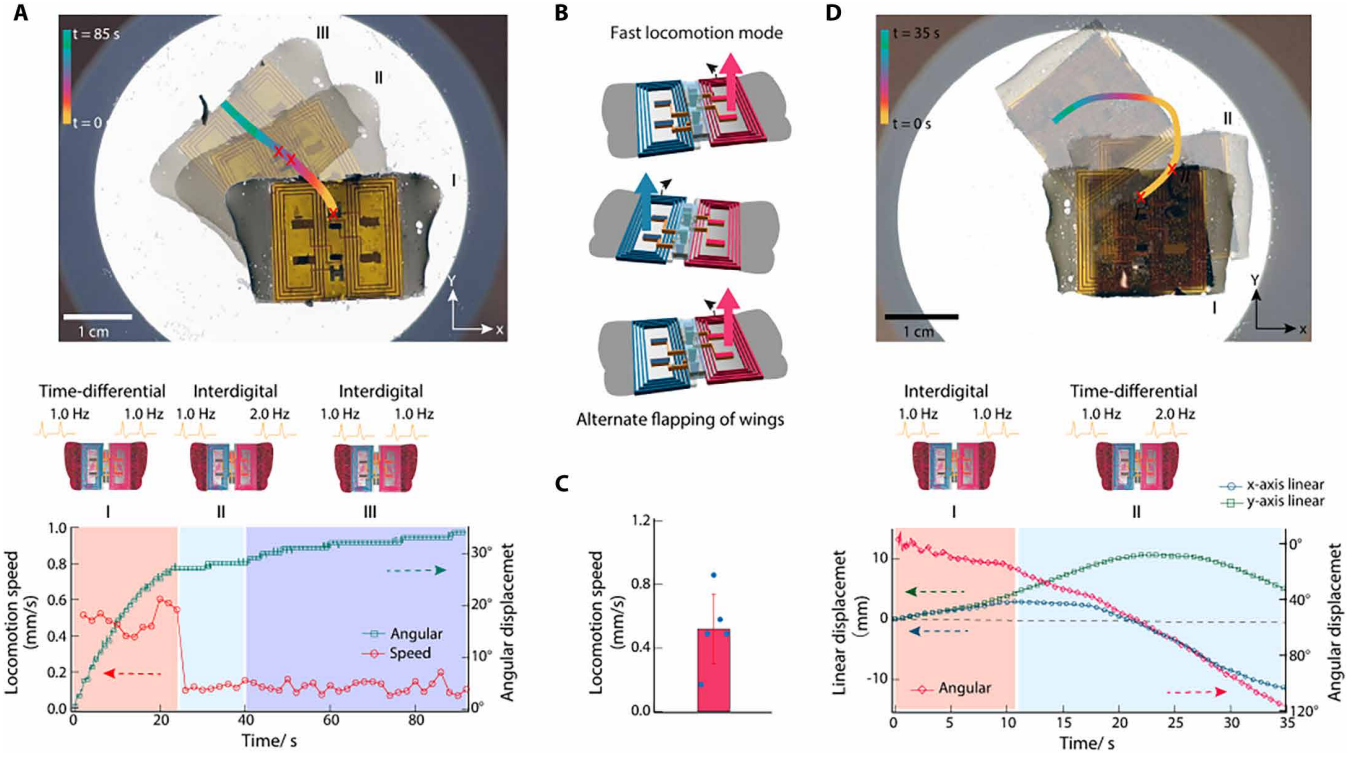

Fig. 7. Locomotion performance of bioelectronic neuromuscular robots. (**A**) The locomotion trajectory of a neuromuscular robot under different transmission signals (V_{sup} = 2.5 V) and varying locomotion speeds. Scale bar, 1 cm. (**B**) Efficient locomotion of robots by alternate flapping of fins. (**C**) Average locomotion speed of neuromuscular robots (n = 5 robots; data represent mean ± SEM). (**D**) The locomotion trajectory of a turning neuromuscular robot and its linear and angular displacements (V_{sup} = 2.5 V). Scale bar, 1 cm.

left and right turning locomotion with an average turning path curvature of ~0.11 ± 0.04 mm^{-1} (movie S15). Figure 7D demonstrates its switching capability of turning controlled through wireless signal modulation (movie S16) to further highlight the robot's maneuverability. The robot's locomotion angle was changed by ~34° by swapping the signal mode to time-differential and the signal frequencies to 1 Hz for the left fin and 2 Hz for the right fin. The robot exhibited a turning locomotion with a turning path curvature of ~0.13 mm^{-1}. These robots' locomotion speed and turning locomotion path curvature were in the same range as the performance of the robot evaluated in a large petri dish with a diameter of 150 mm, where the robot showed a locomotion speed of ~0.73 mm/s and

a turning locomotion path curvature of ~0.07 mm^{-1} (average locomotion speed, ~0.68 ± 0.10 mm/s; and average turning locomotion path curvature, ~0.07 ± 0.02 mm^{-1} for four measurements) (fig. S35). Despite the large variability in the angular displacement between the robots in Fig. 5D, the slight variation in linear displacements and locomotion speeds might result from viscous drag from a larger bioelectronic device part, compensating for the ability to displace fluid masses.

DISCUSSION

In this study, we integrated a motor neurocardiac system and wireless frequency multiplexing bioelectronics into a biohybrid machine and presented their neuronal motion control through wireless signal modulation. We engineered an artificial electrical synapse of iPSC-MNs and iPSC-CMs on a bioelectronic device. This electrical synapse enables a connection between different cell types via a gap junction and faster bidirectional signaling, expanding the flexibility of designing biohybrid systems. A microfluidic device was used to generate electrical synapses through MN-CM coculturing for in vitro analysis of the neuronal connection and functionality of the motor neurocardiac system. MN axons migrated through the microgrooves toward the CM compartment, where they were physically associated with clusters of Cx43 on CMs. Cx-generated gap junctions mediate the electrical coupling and transfer of small molecules. Membrane potential imaging characterization of the functionality of motor neurocardiac junctions showed that CM electrical activities were synchronized with those of electrically stimulated MNs, confirming MN-CM signal transduction. Bidirectional signaling was also confirmed. We implemented these neurocardiac junctions into a flexible wireless circuit board to build a frequency multiplexing wireless neuromuscular robot. The robots were designed and assembled to integrate a flexible PCB-based artificial wireless bioelectronic device with a living neuromuscular tissue actuator. This device had two resonant frequencies for selective neural activation via a frequency multiplexing technique while physically assembling and integrating into a functional biohybrid system. The local electrical stimulation technique, previously investigated for muscle actuators (*4*, *5*, *48*), was incorporated into bioelectronic devices to enable selective cell activation, which was challenging to achieve with conventional electrical stimulation methods. The developed wireless bioelectronic device is operated by planar LC circuits at two resonant frequencies to control the robot's fin motion via the motor innervation of cardiac muscles. We controlled the cardiac muscle contraction with regularities via neurons by preparing arbitrary waveforms, where rectangular pulses (pulse width, 0.2 ms; frequency, 10 Hz) were repeated in ~1-s intervals, and two frequencies were multiplexed. The embodied robotic device platform and design approach enabled remote control powering, frequency switching, and steering of the robot's locomotion speed and angle by independently modulating the robot's left and right fins. The incorporation of electrical synapses allowed robust signaling between the iPSC-MNs and the iPSC-CMs, which exhibited no muscle fatigue over 150 s. The capability of our system to selectively activate cardiac muscle tissue with localized electrical neuron stimulation via electrical synapses will play a crucial role in developing future biohybrid robotics with extended muscle responsiveness and controllability. Neuron innervation networks will enable the selective control of electrically isolated specific muscle patches within multiple arrays assembled on biohybrid machines with reduced energy consumption and enhanced cell signaling, enabling versatile forms and applications of biohybrid machines.

The capability of our system to wirelessly command and control muscle activities through the motor nervous system paves the way for further implementing autonomous functions, such as autonomous actuation and learning, into biohybrid systems to realize adaptive motor patterns in response to environmental stimuli. Given our insight into biological motor control, where the central nervous system plays the role of a generator, a design proposition might be muscle control by brain organoids on wireless bioelectronics with microarray electrodes. For example, brain cortical neurons grown on a multielectrode array can respond to the virtual ball game "Pong" on the basis of electrical stimulation patterns and closed-loop feedback (*49*) and can drive robots to avoid collisions with obstacles (*50*). Incorporating these functional systems into bioelectronic neuromuscular robots could be leveraged to engineer autonomous biohybrid systems capable of advanced adaptive motor control and learning. Implementing autonomous functions via the central nervous system could have a substantial influence as a platform for modifying biological functions, remodeling tissue morphologies, and embodying sensing and learning capabilities, leading to advances in robotics and biomedical fields. The developed system provides a foundation for developing autonomous biohybrid systems capable of advanced adaptive motor control and learning.

MATERIALS AND METHODS

Fabrication of wireless bifrequency bioelectronic devices

Conventional photolithography, etching, and vacuum deposition processes were performed by Multi Circuit Boards Ltd. (Germany) and applied on a trilayer flexible PCB comprising PI (~13 μm)–adhesive (~13 μm)–Cu (~18 μm). This was used to define receiver coils and deposit cell stimulation electrodes and bonding pads for diodes and capacitors (fig. S11). After patterning the Cu foil into the abovementioned structures by photolithography and etching, the coil surface was passivated with a PI layer. Drilling and through-hole plating were applied to create a via hole for closing the inductor loops. Next, after coating another PI layer over the entire structure, the diodes and capacitors were mounted at designated locations. Last, the wireless device was encapsulated using PDMS.

Fabrication of bioelectronic neuromuscular robots

Materials for CNT/gelatin thin film scaffolds and cells

Gelatin from porcine skin (type A, ~300-g bloom) was obtained from Sigma-Aldrich. NanoLab Inc. supplied carboxyl acid–functionalized multiwalled CNTs (30 ± 15 nm in diameter and 5 to 20 μm long). IPS Adhesives Inc. supplied transglutaminase (Moo Gloo TI). Thermo Fisher Scientific Inc. supplied Dulbecco's phosphate-buffered saline (DPBS). FUJIFILM Cellular Dynamics, Inc. supplied single-cell suspensions of iPSC-MNs, iPSC-CMs, and their plating and maintenance media (iCell Motor Neurons Kit and iCell Cardiomyocytes^2 Kit). These iPSC-MNs and iPSC-CMs were differentiated, and we used the cells provided as a single-cell suspension.

Integration of wireless bioelectronic devices into CNT/gelatin thin film scaffolds

Our strategy for fabricating neuromuscular robots is presented in fig. S9. The wireless bioelectronic device was put on a glass substrate

with a mold. Then, 500 μl of 0.1 w/v% CNT/10 w/v% gelatin hydrogel solution was mixed with a transglutaminase solution (mTG; 10 U of mTG per gram) and poured onto the mold. Next, a PDMS stamp with line groove features (0.8-μm groove width and depth each) was attached to the top of the CNT/gelatin hydrogel. A 100-g scale calibration weight was placed onto the PDMS stamp to make a CNT/gelatin hydrogel with a targeted thickness by eliminating excess hydrogel. The CNT/gelatin hydrogel was cross-linked overnight at room temperature (RT) under a glass cover to prevent the hydrogel from completely drying. After hydrogel cross-linking, the weight was carefully removed.

Sterilization protocol of wireless device–embedded CNT/gelatin thin film scaffolds

After embedding the wireless bioelectronic device into the CNT/gelatin thin film scaffolds, the construct was washed with 10% antibiotic-antimycotic DPBS solution (Thermo Fisher Scientific Inc.) and incubated for 10 min at RT. Next, we incubated the construct in a 1% antibiotic-antimycotic DPBS solution overnight at 37°C before seeding the cells.

Culture of iPSC-MNs and iPSC-CMs on the construct

After performing the sterilization protocol, we seeded the iPSC-CMs as a single-cell suspension onto the constructs using a plating medium at a seeding density of ~2.5×10^5 cells/cm^2. After 4 hours of incubation at 37°C, we changed the medium to a maintenance medium. The medium was replaced every other day. After 4 days of iPSC-CM culturing, iPSC-MNs were seeded as a single-cell suspension at a seeding density of ~1.56×10^5 cells/cm^2. The construct was brought to RT before iPSC-MN seeding to suppress the spontaneous beating of iPSC-CMs, ensuring the attachment of the iPSC-MNs onto the cardiac tissue showing spontaneous beating. The iPSC-MNs single-cell suspension was plated onto the construct and allowed to stand at RT for ~20 min to allow the iPSC-MNs to adhere to the cardiac tissue. The iPSC-MNs and iPSC-CMs were cocultured in a 100% maintenance medium of iPSC-MNs for 4 days. Then, the medium was replaced with a 100% maintenance medium of iPSC-CMs, and the medium was replaced every other day.

Immunostaining for cell characterization

For the immunostaining characterization of the iPSC-MNs and iPSC-CMs on the robots, the constructs were washed at RT with DPBS for 5 min and then fixed with 4% paraformaldehyde (Sigma-Aldrich) for 15 min at RT. After washing with DPBS three times at RT for 5 min each, the constructs were washed with 1% bovine serum albumin (Sigma-Aldrich) in DPBS (washing buffer). Next, the constructs were blocked with 0.2% Triton X-100 (Thermo Fisher Scientific Inc.) and 10% normal goat serum (Thermo Fisher Scientific Inc.) in DPBS (blocking buffer) at 4°C overnight. We incubated the constructs with three combinations of two primary antibodies: mouse anti-sarcomeric α-actinin antibody (ab9465, Abcam) and rabbit anti–β-tubulin antibody (ab18207, Abcam), mouse anti–β-tubulin antibody (ab7751, Abcam) and rabbit anti-Cx43 antibody (ab11370, Abcam), or mouse anti–troponin T antibody (ab8295, Abcam) and rabbit anti–β-tubulin antibody (ab18207, Abcam) in the blocking buffer (1:200) at 4°C overnight. After three DPBS washes at RT for 5 min each, goat anti-mouse immunoglobulin G (IgG) AF488 and goat anti-rabbit IgG AF594 secondary antibodies (Thermo Fisher Scientific Inc.) in the blocking buffer (1:200) were added and incubated at RT for 30 min. Subsequently, we incubated the constructs with 4′,6-diamidino-2-phenylindole (Thermo Fisher Scientific Inc.) in DPBS (1:1000) at RT for 15 min. We used an inverted fluorescence microscope (Eclipse TE 2000 U, Nikon) and a laser microscope (LSM 880, Carl Zeiss) to visualize the immunostained cardiac tissues.

Membrane potential imaging

Membrane potential changes in the iPSC-MNs and iPSC-CMs were recorded using an inverted fluorescence microscope equipped with a FLIPR membrane potential assay kit (Molecular Devices LLC.). We incubated the constructs with the dye-loading solution for 30 min and then measured the membrane potential. The change rate in fluorescence intensity was calculated and displayed in pseudocolor using ImageJ Fiji software (*51*).

Cell alignment index

An alignment index was calculated using a custom-made MATLAB (MathWorks, Inc.) code from confocal images, following a previously reported method (*52*). The code calculates the power spectrum of the two-dimensional Fourier image of cells and converts the spectrum to polar coordinates at 1° intervals. Then, it calculates the number-averaged line intensities for each interval angle and determines the alignment index from the matrix eigenvalues. Alignment indices 0 and 1 represent random and perfectly aligned distributions, respectively.

Western blotting

Structural maturation and Cx expression of iPSC-MNs and iPSC-CMs were analyzed by quantifying the relative protein expression levels of β-tubulin, Cx36, Cx43, troponin I, and sarcomeric α-actinin using standard Western blotting techniques. Total vinculin was the loading control in each case. The iPSC-MNs and iPSC-CMs were harvested and lysed in a radioimmunoprecipitation assay buffer supplemented with a protease inhibitor cocktail (Thermo Fisher Scientific Inc.). Cellular disruption was sonicated for 30 min at 4°C. The lysates were then separated by centrifugation at 21,000*g* for 10 min at 4°C. The protein concentration was determined using the Pierce Rapid Gold BCA Protein Assay kit (Thermo Fisher Scientific) following the manufacturer's instructions. Lysates were diluted into a Laemmli buffer (Bio-rad) supplemented with 100 mM 2-mercaptoethanol (Sigma-Aldrich) and heated for 10 min at 90°C; 10 μg of soluble lysate was loaded per well. The proteins were separated using SDS–polyacrylamide gel electrophoresis with 4 to 20% gradient gels (Millipore) and transferred onto a 0.2-μm polyvinylidene difluoride membrane (Thermo Fisher Scientific). After transfer, the membranes were blocked with 5% skimmed milk in PBS at 4°C overnight. The primary antibodies were diluted in the blocking buffer and incubated with membranes for 1 hour at RT under gentle shaking. Anti-vinculin (ab18058, Abcam), anti–β-tubulin (ab18207, Abcam), anti–troponin T (ab8295, Abcam), anti-Cx43 (ab11370, Abcam), anti-Cx36 (ab277766, Abcam), and anti–sarcomeric α-actinin (ab9465, Abcam) were the primary antibodies. The membranes were thoroughly washed with PBST (0.1% Tween 20 v/v PBS) and probed with secondary antibodies. Horseradish peroxidase–conjugated goat anti-mouse IgG (ab6789, Abcam) and anti-rabbit IgG (ab205718, Abcam) were used at a 1:10,000 dilution. Chemiluminescence was detected using a C-DiGit blot scanner, and quantification was performed using Image Studio 5.2 (LI-COR Biosciences).

Mechanical testing of the CNT/gelatin hydrogels

Young's modulus of hydrogels was measured using a UniVert mechanical testing system (CellScale). Hydrogel samples were cut into disks with a diameter of 6 mm and a height of 1 mm. The slope of the stress-strain curve in the linear region was determined as a measure of Young's modulus during the compression test.

Controllability and locomotion assessment of bioelectronic neuromuscular robots

The neuromuscular robots were released in Dulbecco's modified Eagle medium (no phenol red, Thermo Fisher Scientific Inc.) to record their motions and locomotion abilities. We configured function generators (3500B series, Keysight) with RF source switches to deliver target operational signals to the robots that drive the neuromuscular robots and switch transmitting signal modes and intervals. Videos of the neuromuscular robots during neural stimulation were recorded using a digital camera with a macrolens (α6400, Sony). The robot's motions caused by neural stimulations and their positions during locomotion were analyzed from the video recordings using the video analysis and modeling software Tracker (http://physlets.org/tracker). A simulation of the distributions of the applied electrical field potential through the bifrequency wireless device was evaluated using the partial differential equation toolbox of MATLAB.

Optical flow (motion vector) analysis

Optical flow was analyzed through a custom-made MATLAB code from the video recorded during the neural stimulation of robots using a MATLAB computer vision toolbox. We analyzed multiple markers on the robots to inspect the velocity and directionality of each measured portion. The markers were obtained digitally using pixel intensity. Velocity and directionality are the magnitude and direction of the displacement of two consecutive frames, respectively.

Neural spike analysis

We theoretically analyzed the electrical properties of neurons using a leaky integrate-and-fire model to generate action potentials implemented in the MATLAB code, following previously reported methods by I. Cooper (https://d-arora.github.io/Doing-Physics-With-Matlab/mpDocs/pbs007.htm), E. Orhan (https://www.cns.nyu.edu/~eorhan/notes/lif-neuron.pdf), and Gerstner *et al.* (*53*). The electrical properties of the neural cell membrane were modeled as a parallel circuit comprising membrane capacitance C and resistance R in series with a resting potential V_{rest} and driven by external stimuli with a pulse voltage of 0.2 ms.

Finite-element simulations

The deflection behavior of the bioelectronic neuromuscular robots was predicted with finite element simulations using Autodesk Fusion 360 (Autodesk Inc.) on the basis of computer-aided design models of neuromuscular robots and the physical parameters of CNT/gelatin hydrogel. The neuromuscular robots were placed on a support surface (the ground) and allowed to deform in response to the pressure applied to the muscle strips.

Computational fluid dynamics analysis

The flow field the neuromuscular robot experiences in a petri dish was predicted with computational fluid dynamics analyses using Flowsquare$^+$ (Nora Scientific Co. Ltd.). We conducted a flow simulation in a 100-mm-diameter dish with water, with a bioelectronic robot generating water flow in the x direction toward the wall boundary. We set the water flow generated by the bioelectronic robot to 8 mm/s, which is the same velocity field as reported in engineered cardiac tissue constructs of ~6 to 10 mm/s (*2*).

Statistical analysis

The average Cx expression levels (Fig. 2E) were measured for $n = 3$ samples. The average alignment indices (Fig. 3H) were performed for $n = 3$ samples. Relative protein expression levels (Fig. 3I) were performed for $n = 3$ samples. The average reduction in angular displacement (Fig. 5B) was assessed for $n = 3$ robots. The threshold voltages (Fig. 5C) were assessed for $n = 5$ robots for the neurocardiac system and $n = 3$ robots for the cardiac muscle–only system. The average locomotion speed (Fig. 7C) was evaluated for $n = 5$ robots. The average density of neuromuscular robots was measured for $n = 4$ robots (fig. S12C). The average Young's modulus of the CNT/gelatin hydrogels was assessed for $n = 3$ samples (fig. S14D). The average locomotion speed of the cardiac muscle-only system was evaluated for $n = 3$ robots (fig. S26C). The error bars for these measurements represent the SEM. Tukey's multiple comparisons compared the data groups shown in Figs. 2E; 3, H and I; and 5C. The P values and number of samples (n) are provided in the figure captions of the corresponding graphs.

Supplementary Materials

The PDF file includes:
Methods
Figs. S1 to S35
Table S1
References (*54*–*57*)

Other Supplementary Material for this manuscript includes the following:
Movies S1 to S16
MDAR Reproducibility Checklist

REFERENCES AND NOTES

1. K. Y. Lee, S. J. Park, D. G. Matthews, S. L. Kim, C. A. Marquez, J. F. Zimmerman, H. A. M. Ardoña, A. G. Kleber, G. V. Lauder, K. K. Parker, An autonomously swimming biohybrid fish designed with human cardiac biophysics. *Science* **375**, 639–647 (2022).
2. J. C. Nawroth, H. Lee, A. W. Feinberg, C. M. Ripplinger, M. L. McCain, A. Grosberg, J. O. Dabiri, K. K. Parker, A tissue-engineered jellyfish with biomimetic propulsion. *Nat. Biotechnol.* **30**, 792–797 (2012).
3. S. J. Park, M. Gazzola, K. S. Park, S. Park, V. di Santo, E. L. Blevins, J. U. Lind, P. H. Campbell, S. Dauth, A. K. Capulli, F. S. Pasqualini, S. Ahn, A. Cho, H. Yuan, B. M. Maoz, R. Vijaykumar, J. W. Choi, K. Deisseroth, G. V. Lauder, L. Mahadevan, K. K. Parker, Phototactic guidance of a tissue-engineered soft-robotic ray. *Science* **353**, 158–162 (2016).
4. S. R. Shin, B. Migliori, B. Miccoli, Y. C. Li, P. Mostafalu, J. Seo, S. Mandla, A. Enrico, S. Antona, R. Sabarish, T. Zheng, L. Pirrami, K. Zhang, Y. S. Zhang, K. T. Wan, D. Demarchi, M. R. Dokmeci, A. Khademhosseini, Electrically driven microengineered bioinspired soft robots. *Adv. Mater.* **30**, 1704189 (2018).
5. H. Tetsuka, L. Pirrami, T. Wang, D. Demarchi, S. R. Shin, Wirelessly powered 3D printed hierarchical biohybrid robots with multiscale mechanical properties. *Adv. Funct. Mater.* **32**, 2202674 (2022).
6. M. Guix, R. Mestre, T. Patiño, M. De Corato, J. Fuentes, G. Zarpellon, S. Sánchez, Biohybrid soft robots with self-stimulating skeletons. *Sci. Robot.* **6**, eabe7577 (2021).
7. Y. Kim, Y. Yang, X. Zhang, Z. Li, A. Vázquez-Guardado, I. Park, J. Wang, A. I. Efimov, Z. Dou, Y. Wang, J. Park, H. Luan, X. Ni, Y. S. Kim, J. Baek, J. J. Park, Z. Xie, H. Zhao, M. Gazzola, J. A. Rogers, R. Bashir, Remote control of muscle-driven miniature robots with battery-free wireless optoelectronics. *Sci. Robot.* **8**, eadd1053 (2023).
8. R. Raman, C. Cvetkovic, S. G. M. Uzel, R. J. Platt, P. Sengupta, R. D. Kamm, R. Bashir, Optogenetic skeletal muscle-powered adaptive biological machines. *Proc. Natl. Acad. Sci. U.S.A.* **113**, 3497–3502 (2016).

9. Z. Li, Y. Seo, O. Aydin, M. Elhebeary, R. D. Kamm, H. Kong, M. T. A. Saif, Biohybrid valveless pump-bot powered by engineered skeletal muscle. *Proc. Natl. Acad. Sci. U.S.A.* **116**, 1543–1548 (2019).
10. Y. Tanaka, K. Sato, T. Shimizu, M. Yamato, T. Okano, T. Kitamori, A micro-spherical heart pump powered by cultured cardiomyocytes. *Lab Chip* **7**, 207–212 (2007).
11. Y. Morimoto, H. Onoe, S. Takeuchi, Biohybrid robot powered by an antagonistic pair of skeletal muscle tissues. *Sci. Robot.* **3**, aat4440 (2018).
12. F. Fu, L. Shang, Z. Chen, Y. Yu, Y. Zhao, Bioinspired living structural color hydrogels. *Sci. Robot.* **3**, eaar8580 (2018).
13. N. W. Xu, J. O. Dabiri, Low-power microelectronics embedded in live jellyfish enhance propulsion. *Sci. Adv.* **6**, eaaz3194 (2020).
14. S. Ma, P. Liu, S. Liu, Y. Li, B. Li, Launching of a cyborg locust via co-contraction control of hindleg muscles. *IEEE Trans. Robot.* **38**, 2208–2219 (2022).
15. H. D. Nguyen, P. Z. Tan, H. Sato, T. T. Vo-Doan, Sideways walking control of a cyborg beetle. *IEEE Trans. Med. Robot. Bionics* **2**, 331–337 (2020).
16. P. T. Tran-Ngoc, D. L. Le, B. S. Chong, H. D. Nguyen, V. T. Dung, F. Cao, Y. Li, K. Kai, J. H. Gan, T. T. Vo-Doan, T. L. Nguyen, H. Sato, Intelligent insect–computer hybrid robot: Installing innate obstacle negotiation and onboard human detection onto cyborg insect. *Adv. Intell. Syst.* **5**, 2200319 (2023).
17. J. S. Carp, J. R. Wolpaw, "Motor neurons and spinal control of movement" in *eLS* (Wiley, 2010).
18. T. Zaglia, M. Mongillo, Cardiac sympathetic innervation, from a different point of (re)view. *J. Physiol.* **595**, 3919–3930 (2017).
19. R. Gordan, J. K. Gwathmey, L. H. Xie, Autonomic and endocrine control of cardiovascular function. *World J. Cardiol.* **7**, 204–214 (2015).
20. O. Aydin, X. Zhang, S. Nuethong, G. J. Pagan-Diaz, R. Bashir, M. Gazzola, M. T. A. Saif, Neuromuscular actuation of biohybrid motile bots. *Proc. Natl. Acad. Sci. U.S.A.* **116**, 19841–19847 (2019).
21. O. Aydin, A. P. Passaro, M. Elhebeary, G. J. Pagan-Diaz, A. Fan, S. Nuethong, R. Bashir, S. L. Stice, M. T. A. Saif, Development of 3D neuromuscular bioactuators. *APL Bioeng.* **4**, 016107 (2020).
22. L. K. McCorry, Physiology of the autonomic nervous system. *Am. J. Pharm. Educ.* **71**, 78 (2007).
23. N. Matsuhisa, S. Niu, S. J. K. O'Neill, J. Kang, Y. Ochiai, T. Katsumata, H. C. Wu, M. Ashizawa, G. J. N. Wang, D. Zhong, X. Wang, X. Gong, R. Ning, H. Gong, I. You, Y. Zheng, Z. Zhang, J. B. H. Tok, X. Chen, Z. Bao, High-frequency and intrinsically stretchable polymer diodes. *Nature* **600**, 246–252 (2021).
24. D. H. Kim, N. Lu, R. Ma, Y.-S. Kim, R.-H. Kim, S. Wang, J. Wu, S. M. Won, H. Tao, A. Islam, K. J. Yu, T.-i. Kim, R. Chowdhury, M. Ying, L. Xu, M. Li, H.-J. Chung, H. Keum, M. McCormick, P. Liu, Y.-W. Zhang, F. G. Omenetto, Y. Huang, T. Coleman, J. A. Rogers, Epidermal electronics. *Science* **333**, 838–843 (2011).
25. K. I. Jang, K. Li, H. U. Chung, S. Xu, H. N. Jung, Y. Yang, J. W. Kwak, H. H. Jung, J. Song, C. Yang, A. Wang, Z. Liu, J. Y. Lee, B. H. Kim, J. H. Kim, J. Lee, Y. Yu, B. J. Kim, H. Jang, K. J. Yu, J. Kim, J. W. Lee, J. W. Jeong, Y. M. Song, Y. Huang, Y. Zhang, J. A. Rogers, Self-assembled three dimensional network designs for soft electronics. *Nat. Commun.* **8**, 15894 (2017).
26. Y. S. Choi, Y. Y. Hsueh, J. Koo, Q. Yang, R. Avila, B. Hu, Z. Xie, G. Lee, Z. Ning, C. Liu, Y. Xu, Y. J. Lee, W. Zhao, J. Fang, Y. Deng, S. M. Lee, A. Vázquez-Guardado, I. Stepien, Y. Yan, J. W. Song, C. Haney, Y. S. Oh, W. Liu, H. J. Yoon, A. Banks, M. R. MacEwan, G. A. Ameer, W. Z. Ray, Y. Huang, T. Xie, C. K. Franz, S. Li, J. A. Rogers, Stretchable, dynamic covalent polymers for soft, long-lived bioresorbable electronic stimulators designed to facilitate neuromuscular regeneration. *Nat. Commun.* **11**, 5990 (2020).
27. J. Koo, M. R. MacEwan, S. K. Kang, S. M. Won, M. Stephen, P. Gamble, Z. Xie, Y. Yan, Y. Y. Chen, J. Shin, N. Birenbaum, S. Chung, S. B. Kim, J. Khalifeh, D. V. Harburg, K. Bean, M. Paskett, J. Kim, Z. S. Zohny, S. M. Lee, R. Zhang, K. Luo, B. Ji, A. Banks, H. M. Lee, Y. Huang, W. Z. Ray, J. A. Rogers, Wireless bioresorbable electronic system enables sustained nonpharmacological neuroregenerative therapy. *Nat. Med.* **24**, 1830–1836 (2018).
28. M. Boyvat, J. S. Koh, R. J. Wood, Addressable wireless actuation for multijoint folding robots and devices. *Sci. Robot.* **2**, eaan1584 (2017).
29. C. Mc Caffrey, T. Umedachi, W. Jiang, T. Sasatani, Y. Narusue, R. Niiyama, Y. Kawahara, Continuum robotic caterpillar with wirelessly powered shape memory alloy actuators. *Soft Robot.* **7**, 700–710 (2020).
30. M. S. Mohamed Ali, K. Takahata, Wireless microfluidic control with integrated shape-memory-alloy actuators operated by field frequency modulation. *J. Micromech. Microeng.* **21**, 075005 (2011).
31. F. Allen, A. Warner, Gap junctional communication during neuromuscular junction formation. *Neuron* **6**, 101–111 (1991).
32. J. P. Neunuebel, M. J. Zoran, Electrical synapse formation disrupts calcium-dependent exocytosis, but not vesicle mobilization. *Synapse* **56**, 154–165 (2005).
33. M. Wheelwright, Z. Win, J. L. Mikkila, K. Y. Amen, P. W. Alford, J. M. Metzger, Investigation of human iPSC-derived cardiac myocyte functional maturation by single cell traction force microscopy. *PLOS ONE* **13**, e0194909 (2018).
34. C. Wang, M. E. Ward, R. Chen, K. Liu, T. E. Tracy, X. Chen, M. Xie, P. D. Sohn, C. Ludwig, A. Meyer-Franke, C. M. Karch, S. Ding, L. Gan, Scalable production of iPSC-derived human neurons to identify tau-lowering compounds by high-content screening. *Stem Cell Reports* **9**, 1221–1233 (2017).
35. R. P. Rees, M. B. Bunge, R. P. Bunge, Morphological changes in the neuritic growth cone and target neuron during synaptic junction development in culture. *J. Cell Biol.* **68**, 240–263 (1976).
36. C. N. Giachello, P. G. Montarolo, M. Ghirardi, Synaptic functions of invertebrate varicosities: What molecular mechanisms lie beneath. *Neural Plast.* **2012**, 670821 (2012).
37. Q. Chang, M. Gonzalez, M. J. Pinter, R. J. Balice-Gordon, Gap junctional coupling and patterns of connexin expression among neonatal rat lumbar spinal motor neurons. *J. Neurosci.* **19**, 10813–10828 (1999).
38. M. V. Bennett, R. S. Zukin, Electrical coupling and neuronal synchronization in the mammalian brain. *Neuron* **41**, 495–511 (2004).
39. N. J. Severs, A. F. Bruce, E. Dupont, S. Rothery, Remodelling of gap junctions and connexin expression in diseased myocardium. *Cardiovasc. Res.* **80**, 9–19 (2008).
40. Z. Liang, X. Wang, Y. Hao, L. Qiu, Y. Lou, Y. Zhang, D. Ma, J. Feng, The multifaceted role of astrocyte connexin 43 in ischemic stroke through forming hemichannels and gap junctions. *Front. Neurol.* **11**, 703 (2020).
41. A. Urzi, I. Lahmann, L. V. N. Nguyen, B. R. Rost, A. García-Pérez, N. Lelievre, M. E. Merritt-Garza, H. C. Phan, G. J. Bassell, W. Rossoll, S. Diecke, S. Kunz, D. Schmitz, M. Gouti, Efficient generation of a self-organizing neuromuscular junction model from human pluripotent stem cells. *Nat. Commun.* **14**, 8043 (2023).
42. E. J. Tehovnik, A. S. Tolias, F. Sultan, W. M. Slocum, N. K. Logothetis, Direct and indirect activation of cortical neurons by electrical microstimulation. *J. Neurophysiol.* **96**, 512–521 (2006).
43. J. Rapp, P. Braun, W. Hemmert, B. Gleich, Optimal pulse configuration for peripheral inductive nerve stimulation. *Biomed. Phys. Eng. Express* **8**, 025020 (2022).
44. M. Imboden, E. de Coulon, A. Poulin, C. Dellenbach, S. Rosset, H. Shea, S. Rohr, High-speed mechano-active multielectrode array for investigating rapid stretch effects on cardiac tissue. *Nat. Commun.* **10**, 834 (2019).
45. P. C. Antoneli, J. T. Goulart, I. Bonilha, D. D. de Carvalho, P. X. de Oliveira, Heart defibrillation: Relationship between pacing threshold and defibrillation probability. *Biomed. Eng. Online* **18**, 96 (2019).
46. G. Yang, Z. Xiao, X. Ren, H. Long, H. Qian, K. Ma, Y. Guo, Enzymatically crosslinked gelatin hydrogel promotes the proliferation of adipose tissue-derived stromal cells. *PeerJ* **4**, e2497 (2016).
47. D. Gupta, J. W. Santoso, M. L. McCain, Characterization of gelatin hydrogels cross-linked with microbial transglutaminase as engineered skeletal muscle substrates. *Bioengineering (Basel)* **8**, 6 (2021).
48. T. Wang, B. Migliori, B. Miccoli, S. R. Shin, Bioinspired soft robot with incorporated microelectrodes. *J. Vis. Exp.* **28**, e60717 (2020).
49. B. J. Kagan, A. C. Kitchen, N. T. Tran, F. Habibollahi, M. Khajehnejad, B. J. Parker, A. Bhat, B. Rollo, A. Razi, K. J. Friston, In vitro neurons learn and exhibit sentience when embodied in a simulated game-world. *Neuron* **110**, 3952–3969.e8 (2022).
50. A. Novellino, P. D. Angelo, L. Cozzi, M. Chiappalone, V. Sanguineti, S. Martinoia, Connecting neurons to a mobile robot: An in vitro bidirectional neural interface. *Comput. Intell. Neurosci.* **2007**, 12725 (2007).
51. J. Schindelin, I. Arganda-Carreras, E. Frise, V. Kaynig, M. Longair, T. Pietzsch, S. Preibisch, C. Rueden, S. Saalfeld, B. Schmid, J. Y. Tinevez, D. J. White, V. Hartenstein, K. Eliceiri, P. Tomancak, A. Cardona, Fiji: An open-source platform for biological-image analysis. *Nat. Methods* **9**, 676–682 (2012).
52. C. P. Ng, B. Hinz, M. A. Swartz, Interstitial fluid flow induces myofibroblast differentiation and collagen alignment in vitro. *J. Cell Sci.* **118**, 4731–4739 (2005).
53. W. Gerstner, W. M. Kistler, R. Naud, *Neuronal Dynamics: From Single Neurons to Networks and Models of Cognition* (Cambridge Univ. Press, 2014).
54. T. P. Patel, K. Man, B. L. Firestein, D. F. Meaney, Automated quantification of neuronal networks and single-cell calcium dynamics using calcium imaging. *J. Neurosci. Methods* **243**, 26–38 (2015).
55. A. W. Feinberg, A. Feigel, S. S. Shevkoplyas, S. Sheehy, G. M. Whitesides, K. K. Parker, Muscular thin films for building actuators and powering devices. *Science* **317**, 1366–1370 (2007).
56. W. H. Zimmermann, I. Melnychenko, T. Eschenhagen, Engineered heart tissue for regeneration of diseased hearts. *Biomaterials* **25**, 1639–1647 (2004).
57. W. Song, J. Ko, Y. H. Choi, N. S. Hwang, Recent advancements in enzyme-mediated crosslinkable hydrogels: In vivo-mimicking strategies. *APL Bioeng.* **5**, 021502 (2021).

Acknowledgments

Funding: This research was supported by Toyota Motor North America Inc. and partially supported by the National Institutes of Health (R01AR077132 to S.R.S.). S.G. and L.P. were

supported by the Electrical Engineering Department of the HEIA-FR, HES-SO University of Applied Sciences and Arts, Western Switzerland. **Author contributions:** S.R.S. and H.T. conceived and designed the project. H.T. designed the robot, conducted experiments, analyzed data, and wrote the manuscript. L.P. designed and fabricated the wireless system. S.G. characterized and tuned the wireless system. T.H. performed the protein expression analyses. S.R.S. and L.P. edited the manuscript. **Competing interests:** The authors declare that they have no competing interests. **Data and materials availability:** All data required to evaluate the conclusions in the paper are presented in the main manuscript and/or the Supplementary Materials. Additional data are available from the authors upon request. The related data and files for this study have been deposited in Dryad at https://doi.org/10.5061/dryad.pvmcvdnvg.

Submitted 11 January 2024
Accepted 26 August 2024
Published 25 September 2024
10.1126/scirobotics.ado0051

Science Robotics

Wirelessly steerable bioelectronic neuromuscular robots adapting neurocardiac junctions

Hiroyuki Tetsuka, Samuele Gobbi, Takaaki Hatanaka, Lorenzo Pirrami, and Su Ryon Shin

Sci. Robot. **9** (94), eado0051. DOI: 10.1126/scirobotics.ado0051

Editor's summary

Typically, biohybrid machines built from cardiac muscle cells have relied on the involuntary, contractile actuation of the cells to continuously propel the robot. However, without the nervous system, this rhythmic pumping action could not be adjusted or controlled. To imbue control, Tetsuka *et al.* developed a biohybrid swimmer with a neurocardiac muscle junction. Acting as an artificial brain, a frequency multiplexing wireless system was used to stimulate the motor neurons, which in turn activated the cardiac muscle cells. The robot's speed could be controlled by modulating the frequency and pulse duration of the electrical signal, and direction was altered by transmitting signals to the left and right fins independently. —Melisa Yashinski

Science Robotics (ISSN 2470-9476) is published by the American Association for the Advancement of Science. 1200 New York Avenue NW, Washington, DC 20005. The title *Science Robotics* is a registered trademark of AAAS.